

GNSS Interference in Unmanned Aerial Systems

Wim De Wilde, Gert Cuypers, Jean-Marie Sleewaegen, Richard Deurloo, Bruno Bougard
Septentrio Satellite Navigation, Belgium

BIOGRAPHIES

Wim De Wilde (M.Sc. in EE) works as a system architect, with focus on the RF and digital signal processing section.

Dr. Gert Cuypers (M.Sc. and Ph.D in EE) works on the receiver RF front-end and antennas.

Dr. Jean-Marie Sleewaegen (M.Sc. and Ph.D in EE) is responsible for the GNSS signal processing, system architecture and technology development.

Dr. Richard Deurloo (M.Sc. in Aerospace Engineering and Ph.D. in Surveying Engineering) works on high-precision GNSS and GNSS/INS integration algorithms.

Dr. Bruno Bougard (M.Sc. and Ph.D in EE) is R&D Director, in charge of research, development, and engineering.

ABSTRACT

This paper discusses interference issues in Unmanned Aerial Systems (UAS) and addresses the benefit of advanced monitoring and mitigation capabilities built into the GNSS receiver module.

First the paper discusses experimental results of interference of UAV electronics into the GNSS sensor. The analysis is based on a specific RF signal monitoring technique built into the receiver module. Several ways to mitigate this self-interference are discussed.

Furthermore the impact of various types of jammers on GNSS reception is experimentally analyzed. A recorded UAV flight is recreated with an RF constellation simulator, adding interference from various jammer types. The interference level is controlled according to electromagnetic propagation laws, taking into account the attitude of the UAV and its antenna radiation pattern.

In this way we evaluated the performance of several receivers under jamming exposure, proving effectiveness of advanced interference mitigation.

INTRODUCTION

The GNSS sensor is a vital part in the large majority of unmanned aerial systems. It is commonly used to guide UAVs, making sure it follows the pre-defined flight path. Most professional UAVs operate autonomously. If the GNSS position is lost, the UAV will still be stabilized by its inertial sensors, but it will be unable to navigate towards its landing spot without intervention of a human operator. Often this would simply lead to loss of the UAV and its payload.

The precision of the navigation solution is also important. For guidance this mainly holds for complex flight phases such as landing. Landing has demanding precision requirements. For fixed-wing UAVs, altitude inaccuracies of 1 m lead to about 10-m inaccuracy on the landing spot. Rotorcrafts are typically supposed to operate from well-defined spots, and meter-level navigation inaccuracies could lead to collisions with surrounding objects.

The most common application for professional UAS is aerial mapping. Camera images are used to create a precise three dimensional model of an area, e.g. to monitor progress of the works in a mining pit or construction yard. Aerial mapping used to require a large number of manually-surveyed reference points on the ground, but there is a trend to eliminate these by moving the high precision positioning to the UAV. The GNSS sensor is synchronized with the camera shutter and cm-accurate geo-tags are created for each picture.

High precision navigation requires phase based techniques. Most aerial mapping UAS use dual frequency (L1/L2) RTK receivers, as these have the ability to instantaneously provide a reliable cm-accurate position. Phase based positioning techniques require good signal availability and quality (C/No). Ensuring this in interference rich environment UAVs typically operate is a challenging task.

The article is organized as follows: first we explain the architecture of the receiver used in the experiments. Next

we discuss the problem and mitigation of self-interference. This is followed by a section on alien interference and a description of the influence of the geometry on the susceptibility. Finally, we present a case study of a simulated flight in the presence of different types of jammers and the effect they have on different types of receivers.

RECEIVER ARCHITECTURE

The analysis and tests discussed in this paper were made with the Septentrio's AsteRx4 multi-frequency RTK/PPP receiver modules. This module supports all L1, L2 and E5/L5 signals from all constellations.

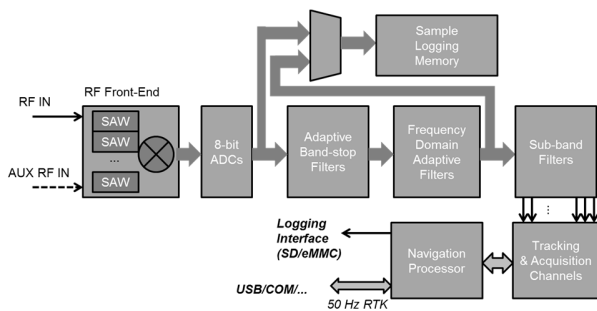


Figure 1: Septentrio's AsteRx4 receiver architecture

This module is specifically designed for operation in harsh interference environments. The antenna signal is down-converted in a multi-channel two stage heterodyning front-end with sharp surface acoustic wave (SAW) filters to reject out-of-band interferers. The output signals are quantized by multi-bit ADCs. The receiver has a built-in capability to log a batch of raw RF signal. The logged samples can be used to detect and study signal anomalies, both in the time and frequency domain.

The digitized GNSS bands are automatically cleaned from interference by multiple adaptive band-stop filters. Their stop-band bandwidth is adjusted automatically between a notch of a few kHz to a MHz-wide rejection, depending on the nature of the interference.

The notch filters are complemented by an adaptive filter capable to reject more complex types of interference such as chirp jammers and frequency hopping interference like DME/TACAN [1]. The receiver also supports regular blanking [2, 3].

The sub-bands (GPS L1, L2, L5; GLONASS L1, L2; GALILEO E1, E5; BeiDou B1, B2) are extracted by sub-band filters, which isolate them from residual interference in adjacent GNSS bands.

The recovered signals are further processed in a large matrix of tracking channels, capable to simultaneously

process all satellite signals in all received bands, even after the emerging constellations (e.g. GALILEO) will be completed.

The collected measurements enter the navigation processor, which computes a high-rate RTK, PPP or SBAS-aided position depending on the corrections provided to the receiver. The measurements can also be logged onto flash memory (SD/eMMC) for replay or post processing, along with the time tag of event-triggers. The latter is particularly interesting for aerial geo-tagging applications, as it eliminates the need to uplink differential corrections to the UAV during the complete flight. RTK accuracy can then be achieved by post-processing of the logged GNSS measurements and photographs meta-data be edited a posteriori.

SELF-INTERFERENCE

An important source of interference is the UAV itself. The limited space available in UAVs causes the GNSS antenna to be physically close to the on-board electrical and electronic systems. This makes it vulnerable to electromagnetic compatibility problems, which could reduce overall receiver performance.

Figure 2 depicts a typical UAV system. An obvious radiation source is the radio modem used for telemetry. However, its fundamental frequency is at least a few hundred MHz from the GNSS bands and even though the power radiated into the GNSS antenna can be very significant (-20 dBm), interference can be mitigated with proper RF filters in the antenna and receiver.

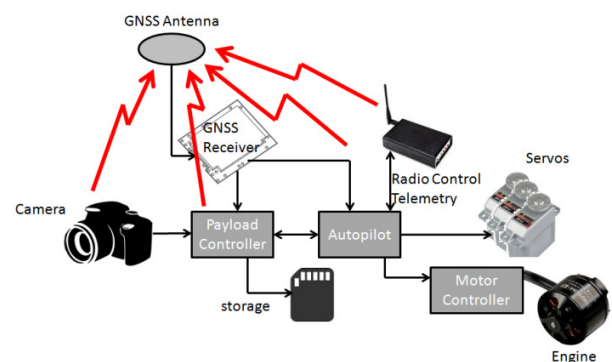


Figure 2: Typical UAV electronic systems

Unintentional emissions are much more of a concern, as they could occur within the GNSS bands. For regulatory approval, the electrical field strength (E) measured at a 3-m distance from the device as produced by spurious emissions such as clock harmonics typically has to be below 500 $\mu\text{V/m}$ [4]. The corresponding power which would be picked up in an isotropic antenna equals:

$$P = \frac{E^2}{R_0} \cdot \frac{\lambda^2}{4\pi}$$

In which R_0 is the free-space impedance of 377 ohm and λ is the applicable wavelength. At the GPS L1 wavelength of 19 cm, this results into a power level of -87 dBm. This is far above the levels at which GNSS signals start to show some level of degradation, which is between -100 and -120 dBm, depending on the specific signal and spectral location of the interference. In a UAV the GNSS antenna is usually much closer than 3 m from the electronics. This results in even higher field strengths, even when taking into account that the antenna will provide some rejection. Often the antenna will be exposed to near field components.

These emissions could originate from unexpected sources. This is illustrated in [Figure 3](#). A receiver module was integrated with a GoPro Hero 2 camera on a F450 quadcopter frame to test the UAS extension board functionality. The GNSS antenna was relatively close to the camera. The L1 C/A C/No turned out to be 12 dB lower than expected and didn't allow an RTK fix. The receiver was logging RF samples, and replaying the log-file in the graphical user interface pointed at an interference issue, as can be seen in [Figure 3](#).

Three peaks with similar shape are visible in the spectrum at 1559 MHz (cut by antenna), 1583 MHz and 1607 MHz, on top of a shaped noise. These frequencies are exactly 24 MHz apart and 1583 MHz is close to the 66th harmonic of a 24 MHz signal. This is a strong indication that an (inaccurate) 24-MHz digital signal is causing the peaks. This is a typical frequency for MMC/SD logging interface, suggesting the issue is caused by a continuously operating flash card interface.

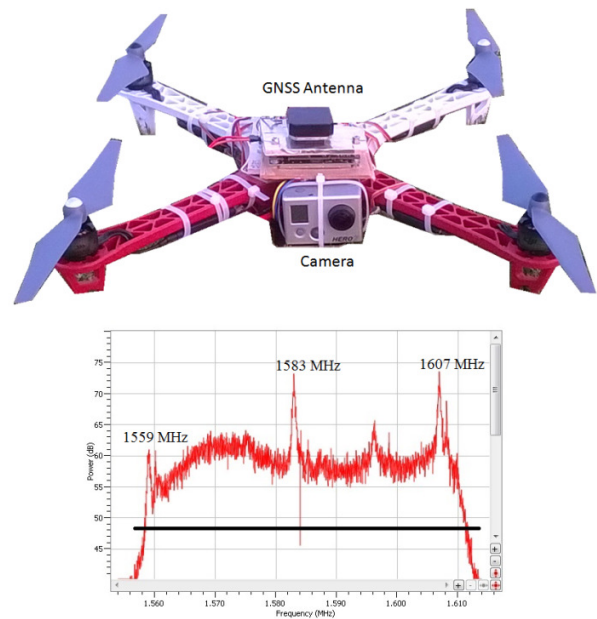


Figure 3: GoPro Hero 2 pick-up monitored by AsteRx4

Indeed, the peaks disappeared when the camera was switched off. When fixing the AGC gain of the receiver and again switching on the camera, the in-band noise reported by the receiver increased with 12 dB. Hence, the antenna was subjected to digital noise of the camera which completely dominated the usual sky thermal noise. This explains the odd-shaped noise profile in the picture and the C/No drop. The radiated noise only reached acceptable levels when the antenna was held more than 40 cm from the camera. In this particular case, the issue was solved by shielding the camera case and putting the antenna on a stick. The issue could also be solved by putting the camera underneath the drone, using the power planes of the drone as a shield.

In a more recent version of the camera the spectral peaks disappeared and the spectrum seems to be mostly clean ([Figure 4](#)). However, the corresponding time domain plot below shows a highly non-stationary signal. It causes a similar C/No degradation as the earlier version. The non-stationary signal is indicative for interference from a high-speed digital interface, for example from bursts associated to digital transfer cycles (e.g. cache line fill from dynamic memory). These bursts contain quasi random data, switching at frequencies above 100 MHz. The pulses give rise to a broad high-pass filtered sinc-like spectrum, extending to frequencies of several GHz. This case stresses the importance of a time domain plot when tracing interference issues. This plot could also be used to debug the interference issue in a lab, without the need for GNSS signals.

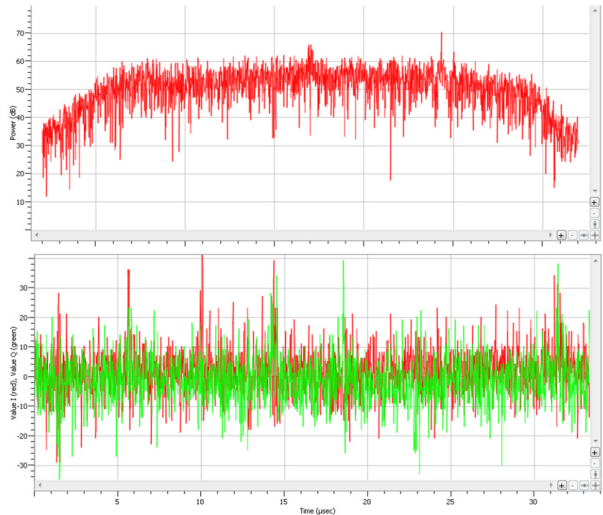


Figure 4: Camera pick-up. Top: L1 spectrum. Lower panel: time series of I (red) & Q (green) ADC samples.

Sometimes digital interference can be mitigated with pulse blanking. In one case, the receiver and a payload containing a CPU and DDR were mounted without shielding under a microstrip antenna with large ground plane. The spectrum showed a large PSD increase towards lower L2 frequencies (red curve, [Figure 5](#), top). The time domain signal was showing many bursts of spikes, pointing at the DDR memory interface in the processing system of the payload. There were also peaks at 24 MHz harmonics, corresponding to the payload logging interface.

The histogram of the magnitude of the complex signal samples is in the bottom plot of [Figure 5](#). We recognize a Rayleigh distribution, but its tail is much longer than normal. This tail corresponds to the pulsed interference of the DDR interface. When blanking the tail with threshold equal to 17, the spectrum reaches normal levels. The signal was blanked during 14% of the time, reducing C/N₀ with slightly more than 1 dB.

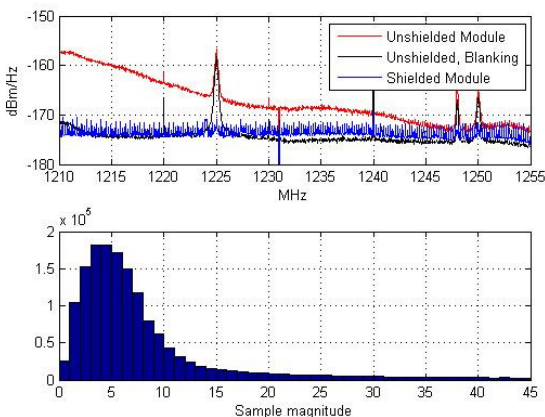


Figure 5: Cleaning DDR interference (red) with blanking (black) and shielding (blue)

When shielding the module, the spurs dramatically reduce (blue curve, [Figure 5](#), top). The blue spectrum still shows many small peaks at 450 kHz spacing, which are 2-3 dB above the background noise. The 450-kHz frequency corresponds to the switching frequency of a switched mode power supply on the host board which integrates the receiver module.

Narrow band interference spikes originating from system clocks or power electronics are very common. Another example is in [Figure 6](#), showing interference from a Sony compact camera into a GPS antenna mounted above the camera at 10-cm distance. The camera generates a spurious emission at 1567 MHz, in the L1 GPS band. This saturates the tracking channels and reduces C/N₀ by 5 dB. Because of the narrow-band nature of the interference, it could be mitigated with a notch filter in the receiver. The bottom plot shows the residual interference using samples behind the interference mitigation. The notch filter increases C/N₀ with 3 dB in this case ([Figure 7](#)). The remaining performance loss is due to wideband digital interference.

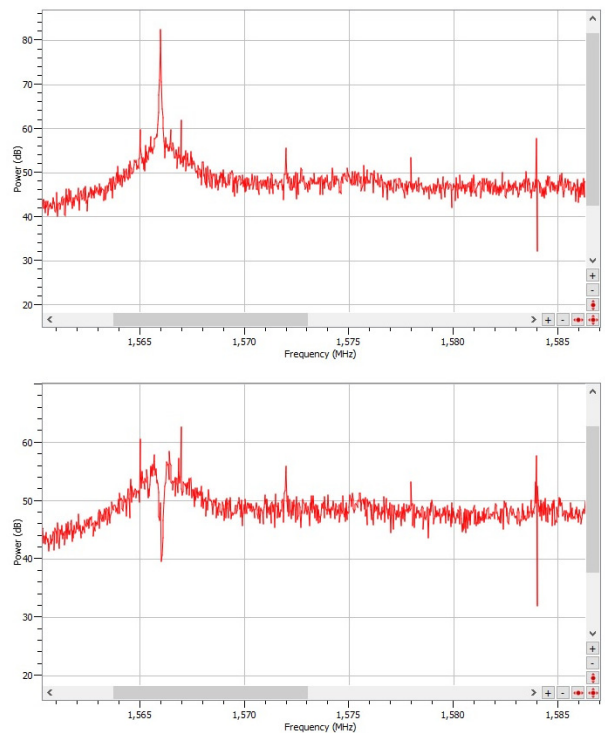


Figure 6: Compact camera interference spectrum before (top) and after (bottom) mitigation

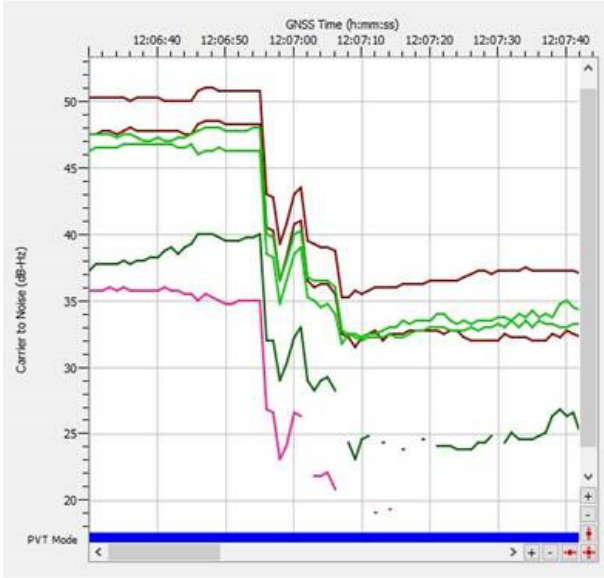


Figure 7: Compact camera impact on C/N₀. A C/N₀ drop of more than 10dB is observed when the camera is active.

The laptop or tablet PC used to monitor the UAV could be another source of cross-talk during take-off. We have seen multiple laptops and tablets radiating a dithered clock into the L1 spectrum. [Figure 8](#) shows an example of a laptop jamming the lower GLONASS L1 band, raising the noise floor with 8 dB. The laptop was at 2 meters from the GNSS antenna in this case. The frequency corresponds to a standard DDR3 memory frequency. The clock is dithered to spread its power spectral density over several MHz in order to meet regulatory approval.

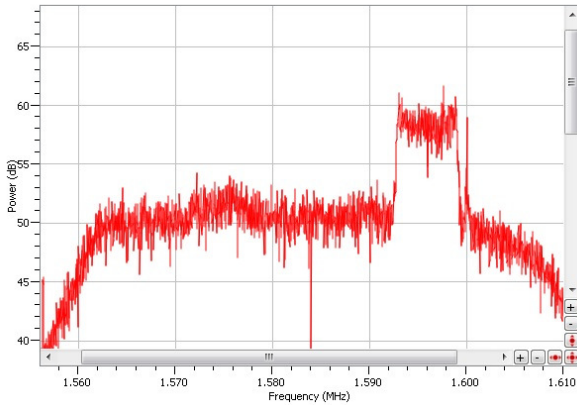


Figure 8: Laptop jamming L1 GLONASS

EXTERNAL INTERFERENCE

Even after a clean integration, UAVs may be exposed to high levels of in-band GNSS interference during their

flight. Typical sources of interference are radio amateur equipment operating in the 23-cm band, spurious emissions of terrestrial radio systems and GPS jammers. Jammers are a particular threat as they are specifically designed to disable GPS reception. Jamming devices, although illegal to operate, are rather easy to procure and are increasingly used in road vehicles [5, 6], in order to disable vehicle tracking. If a vehicle equipped with a GPS jammer crosses the flight track of an UAV, it could impact its navigation. Besides, it is not unlikely that jammers will be used intentionally by people with malicious intentions to bring down a UAV.

PROPAGATION PHYSICS

Airborne GNSS receivers will generally be more likely to be in line of sight of an interfering jammer than terrestrial receivers. Hence, the Friis transmission equation can be applied to calculate the jamming power level P_R at the output of the victim GPS antenna element:

$$P_R = P_J \cdot G_J(\varphi_J, \theta_J) \cdot G_G(\varphi_G, \theta_G) \cdot \left(\frac{\lambda}{4\pi \cdot \|\vec{r}_J - \vec{r}_A\|} \right)^2 \cdot p \quad (1)$$

In which:

- P_J is the power transmitted by the jamming device.
- G_J is the power gain of the jamming antenna at azimuth angle φ_J and bore sight angle θ_J , corresponding to the direction of the UAV in the reference frame of the jamming antenna ([Figure 9](#)).
- G_G is the power gain of the jamming antenna at azimuth angle φ_G and bore sight angle θ_G , corresponding to the direction of the jammer in the reference frame of the UAV antenna.
- λ is the wavelength of the applicable GNSS band.
- $\|\vec{r}_J - \vec{r}_A\|$ is the distance between the jamming antenna and the GNSS antenna
- The parameter p accounts for the polarization loss and can be calculated as $p = \left| \vec{a}_J(\varphi_J, \theta_J) \cdot \vec{a}_G(\varphi_G, \theta_G) \right|$, in which \vec{a}_J and \vec{a}_G are the polarization vectors of the jamming antenna and the GNSS antenna.

During level flight, the jammer will be at negative elevations with respect to the GPS antenna and G_G will be much smaller than one (-5 to -20 dBi), providing some rejection. This rejection depends significantly on the antenna type. Some antennas provides more than 20 dB rejection over a large part of the lower hemisphere, others are limited to 5 dB.

However, when banking (during turns), the jammer could appear at bore sight angles lower than 90° and antenna gain could even boost the signal. It should be noted that the antenna gain pattern also includes the impact of the UAV fuselage and electronics. This impact could be low in small UAVs with foam fuselage, but can be important in larger platforms out of polycarbonate or fiberglass.

Jammers are usually equipped with monopole antennas. When used in a vehicle, the transmitted signal will be reflected at many nearby structures and the effective radiation pattern will get very erratic due to constructive and destructive interference. If the jammer antenna is mounted on a roof, the pattern would be a classical monopole pattern with 5 dBi gain towards the horizon ($\theta_J = 90^\circ$) and with a linearly polarized electrical field proportional to $\frac{\cos(\frac{\pi}{2} \cos(\theta_J))}{\sin(\theta_J)} \cdot \vec{e}_{\theta_J}$

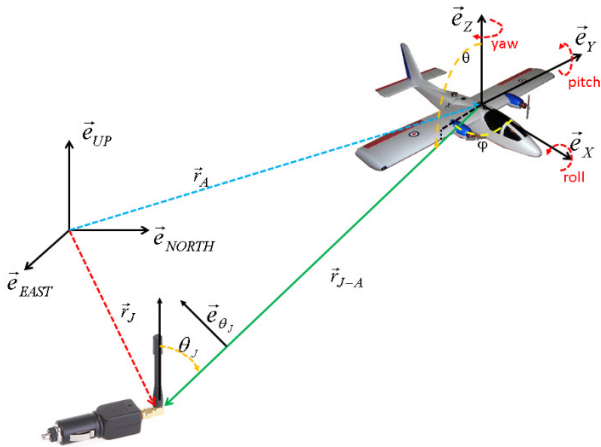


Figure 9: Reference frame definition

Figure 10 shows the idealized gain pattern of the jamming antenna along with the L1 gain pattern of a small dual frequency QFH GNSS antenna as a function of the boresight angle. This GNSS antenna is very popular in UAV applications because of its low weight. In the upper hemisphere the right hand circularly polarized (RHCP) gain is much larger than LHCP gain, yielding optimal GNSS reception. In the lower hemisphere the LHCP reception becomes dominant. The RHCP and LHCP gain also depend on azimuth angle ϕ_G , but the variation is low.

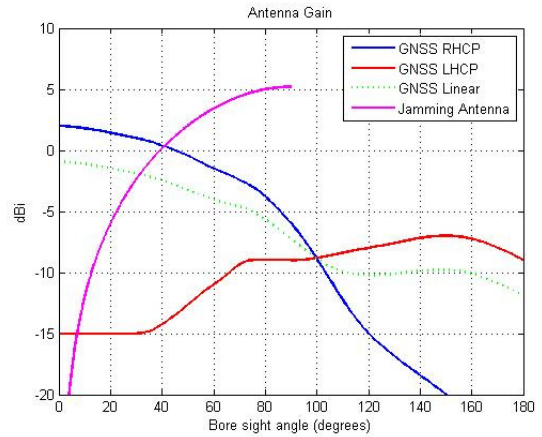


Figure 10: Radiation pattern of QFH L1/L2 antenna and jamming antenna

At 100° bore sight angle the polarization of the GNSS antenna is linear, as RHCP gain equals LHCP gain. The orientation of the polarization vector depends on the precise antenna design. In microstrip antennas it will be along the \vec{e}_{θ_G} axis. If it aligns with the polarization vector of the jamming antenna, the factor p in formula (1) will be one. If orthogonal, it rejects the interference. In the bore sight angle areas with dominant circular polarization, only half of the jamming power would be picked up ($p = 1/2$). The dotted curve in Figure 10 represents the linear gain of the GNSS antenna. It does not depend much on azimuth as it follows the dominant polarization. It equals the gain with which the jamming will be picked up if the polarization ellipse aligns with the polarization of the jamming (worst case situation).

CASE STUDY

The impact of different types of jammers was analyzed using recorded flight data. The flight was recorded with a converted twin engine hobby plane (Figure 9), which carried a GPS receiver, an attitude reference system and an autopilot. The flight consisted of a remote controlled take off, followed by several kilometers of way-point controlled automatic flight over a flat agricultural area. Upon return the UAV started flying perfect circles over the take-off sight, after which the plane was manually landed. The flight track and the associated altitude above ground is shown in Figure 11, with the auto piloted phase in solid line.

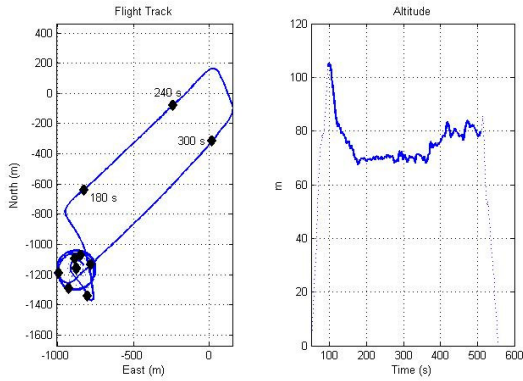


Figure 11: Flight track and altitude above ground

The GPS position and roll, pitch and yaw Euler angles were logged, following the aircraft principle axis conventions. The aircraft position \vec{r}_A in an ENU reference frame could be combined with a hypothetical jammer location \vec{r}_J to work out the corresponding jamming power as according to formula (1). With the conventions of Figure 9, the bore sight and azimuth antenna angle needed to calculate GNSS antenna gain in the jammer direction could be calculated according to the following formulas:

$$\theta_G = a \cos\left(\frac{(\vec{r}_J - \vec{r}_A) \cdot \vec{e}_Z}{\|\vec{r}_J - \vec{r}_A\|}\right)$$

$$\varphi_G = \arg((\vec{r}_J - \vec{r}_A) \cdot (\vec{e}_X + j \cdot \vec{e}_Y))$$

For these calculations the $\vec{r}_J - \vec{r}_A$ vector has to be represented in the XYZ-antenna reference frame attached to the aircraft. This can be calculated by applying the following rotation matrix to the ENU coordinate [7]:

$$R = \begin{bmatrix} s(y)c(r) - c(y)s(p)s(r) & c(y)c(r) + s(y)s(p)s(r) & -c(p)s(r) \\ -c(y)c(p) & -s(y)c(p) & s(p) \\ s(y)s(r) + c(y)s(p)c(r) & -c(y)s(r) - s(y)s(p)c(r) & c(p)c(r) \end{bmatrix}$$

in which $c(\dots)$ and $s(\dots)$ represent the cosine and sine function respectively and y , p and r refer to the yaw, pitch and roll angles of the UAV.

For jamming power calculation, the antenna radiation patterns from Figure 10 were used, reducing the jamming antenna gain with 2 dB to simulate efficiency and misalignment losses. The azimuth dependency was neglected, as it is insignificant.

If a 10-mW jammer would be in the origin of Figure 11, Figure 12 shows the resulting jamming power during the auto piloted phase (bottom) together with the roll and pitch angles. Note the power increases during the turns in the far end of the track because the 30° degrees banking angle

moves the jammer to positive elevations. The same effect is visible during the circling at the end of the flight.

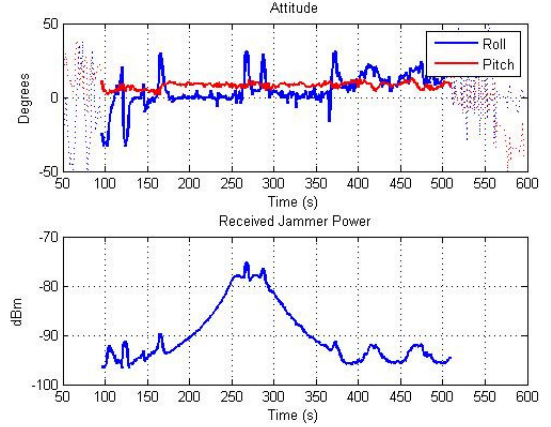


Figure 12: Attitude and received jamming power during flight

The maximal power the receiver antenna is exposed to is -76 dBm. One could wonder how much this power depends on the location of the jammer. Figure 13 shows the highest level the UAV would be exposed to along its track (black) as a function of the jammer location. The level exceeds -80 dBm for any jammer location in an area of more than a square kilometer.

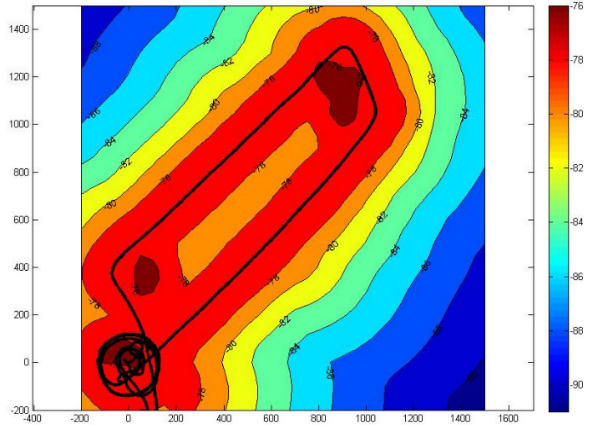


Figure 13: Maximal received jamming power as function of jammer location

Hence, the precise location of the jammer does not have a big impact on the maximal exposure level. The jammer has to be several kilometers away from the track to reach levels equal to the thermal noise power and more than 10 km from the flight track to reach levels which are not significantly affecting GPS signals. For a terrestrial system this would be beyond the radio horizon, meaning that the earth curvature would provide protection if the signal is not already attenuated by surrounding objects. For a typical UAV altitude of 70 m above ground, the radio horizon is at 35 km. Therefore jammers could affect UAV operation over a very wide area.

TEST SETUP

In order to study the impact of jammers on UAVs, the flight track discussed in the previous section was reproduced with a Spirent L1/L2 GPS RF constellation simulator, using recent GPS almanac data to define the constellation. The radiation pattern of the QFH L1/L2 antenna was modelled accurately to correctly simulate GPS power during turns. The test also included a jamming source, which was attenuated with a programmable attenuator to bring it to the precomputed jamming level. This was combined with the GPS signal from the simulator and the resulting signal was provided to the receiver.

Figure 14 provides a more detailed overview of the test set-up. The simulator signal was amplified with an external LNA to simulate an active antenna. The interference power was calibrated using the build-in spectrum analyzer of the receiver, using the -174 -dBm/Hz noise floor as a reference. The simulator output was adjusted to match the theoretical C/N_0 values.

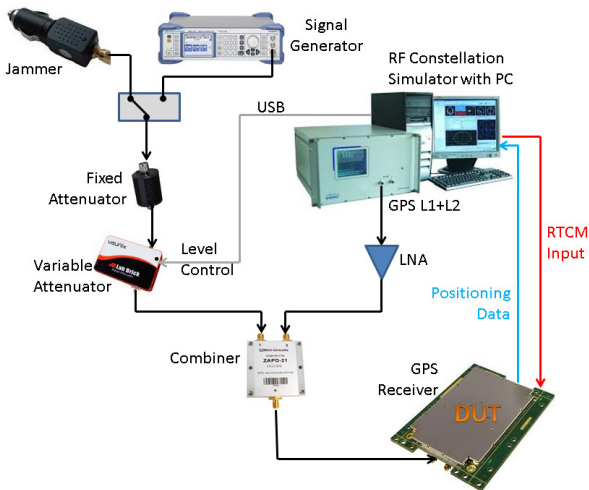


Figure 14: Interference simulation set-up

The simulator was providing RTCM data towards the receiver, in order to let it achieve an RTK position fix.

It was important to precisely synchronize the attenuator control with the simulation. For this the simulator's NMEA time tag was used as an index in a table with pre-computed attenuation settings and the corresponding value was immediately applied to the attenuator.

CHIRP JAMMERS

The impact of chirp jammers was analyzed to evaluate the effectiveness of the adaptive filter in the AsteRx4 receiver. These jammers output a sinewave within the GNSS bands

with rapidly changing frequency. Typical sweep periods are in the order of $10 \mu\text{s}$.

Two jammer devices were used in the test. The first one was a simple low cost L1 chirp jammer with 10-dBm power output. Its spectrum is the black line in Figure 15. It perfectly overlaps with the GPS L1 spectrum

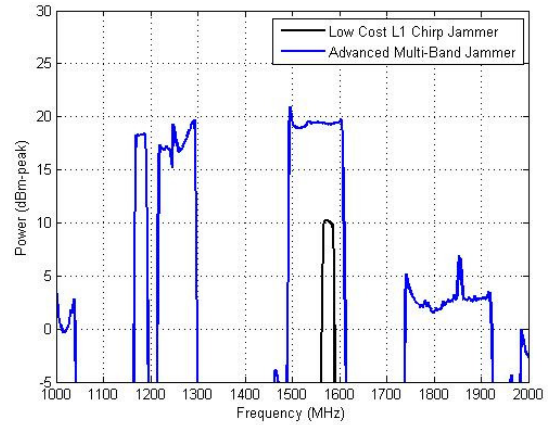


Figure 15: Chirp jammer output spectra

The power output level was measured with a lab spectrum analyzer, using minimal sweep time (Figure 15). It was confirmed with the build-in signal analyzer of the receiver, by first feeding the chirp jammer signal into the receiver and then adjusting a CW generator signal to produce the same RMS level in the time domain plot (Figure 16). The chirp jammer has a remarkable time domain waveform. We have seen this kind of signals many times in field recorded data, confirming the frequent presence of these kind of jammers.

The repeatable nature of the test enabled us to evaluate several receiver types. We evaluated the AsteRx4 receiver both in L1/L2 RTK mode and in L1 stand-alone mode. Besides, we tested a high-end RTK receiver from another brand which is frequently used in UAVs. We also tested a standard L1 receiver which is popular in low end and hobby UAVs.

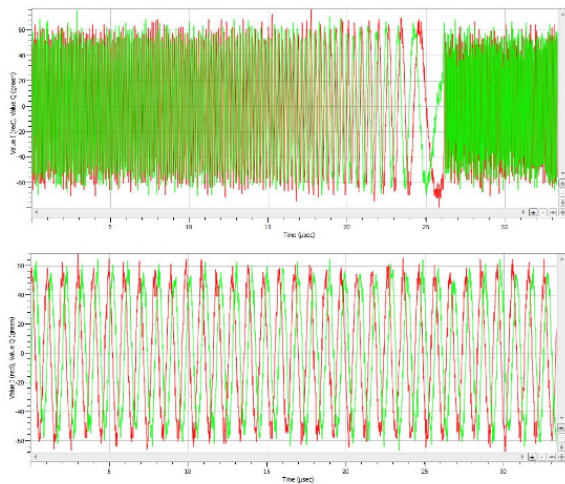


Figure 16: Time-domain signal of chirp jammer (top) and CW with equal power (bottom) measured with AsteRx4

The AsteRx4 receiver shows a correct flight track in both positioning modes (Figure 17). The jammer location is in the origin of the plot. The other high precision receiver loses track when approaching the jammer and only recovers near the end of the flight. The standard L1 receiver performs better, but still loses track during several hundred meters in the flight and wouldn't have been able to safely guide the UAV.

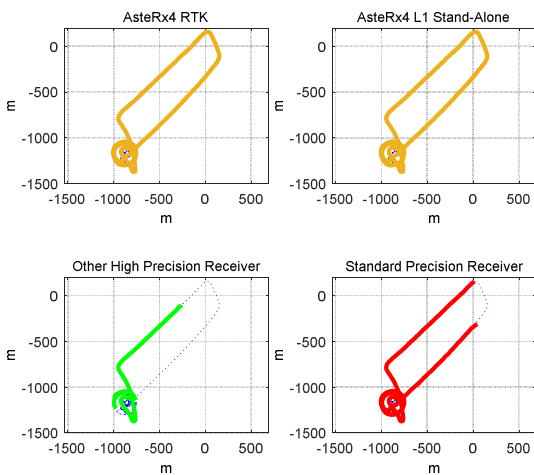


Figure 17: Flight track when exposed to 10-mW L1 chirp jammer. Jammer is at (0, 0)

The corresponding 3D error was calculated for each of the tracks, using the simulated track as a reference (Figure 18). The AsteRx4 receiver achieves cm-level accuracy all the time, proving it was able to maintain a correct RTK fix. In L1 stand-alone mode the positioning error is usually less than 0.5 m and does not depend on the jammer. The other high-end receiver shows a short period of dm-accuracy

before losing navigation. The standard L1 receiver outputs a degraded position during a large part of the track, with over 10-m error when it is reacquiring or when it is about to lose the signal.

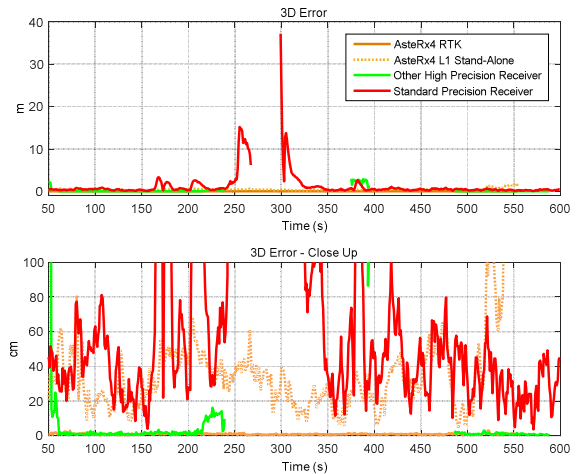


Figure 18: 3D positioning error (chirp jammer)

Figure 19 shows the C/No of a high-elevation satellite during the test for all involved receivers. The jammer switches on just before 100 seconds in the flight. The AsteRx4 receiver shows about 2-dB C/No reduction. The other high precision receiver shows a 5-dB drop. The L1 receiver initially doesn't show a C/No degradation, probably because its lower bandwidth rejects part of the chirp sweep. However, when the UAV gets closer to the jammer and levels exceed -85 dBm (Figure 12), its C/No rapidly drops and eventually the signal is lost. In contrast, the AsteRx4 receiver shows a steady C/No, even during highest exposure, proving effective operation of the adaptive filter.

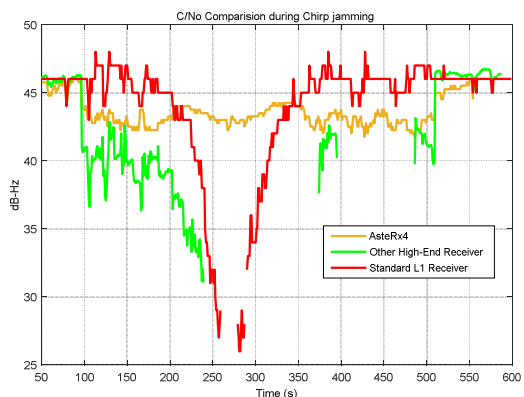


Figure 19: C/No during chirp jamming

After these tests a second type of chirp jammer was evaluated. This handheld jammer is much more expensive, but it can jam multiple GNSS bands (blue line, [Figure 15](#)) in parallel. It transmits four chirp waveforms, each with a dedicated monopole antenna. The chirp generator which targets the higher GNSS band is very wide, sweeping from 1500 to 1600 MHz. Therefore its time domain wave form captured by AsteRx4 shows a pulsed interferer, because part of the sweep is rejected by the front-end filters ([Figure 20](#)). It is further rejected in back-end filters, reducing the duty cycle to 25%.

In the test the outputs of the jammer were joined with an RF combiner and sourced to the receiver via an attenuator.

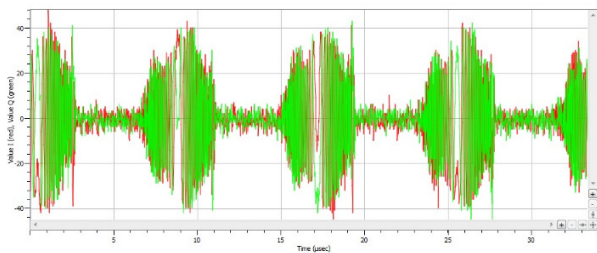


Figure 20: Advanced chirp jammer, time domain signal

As shown in [Figure 21](#), the flight tracks of AsteRx4 are correct, both in stand-alone and RTK mode, with good fix quality. This time, the standard L1 receiver perceives little impact from the jammer, even though the jamming power is considerably higher. This is because the extremely wide L1 sweep gets translated into a low duty cycle pulsed interferer by its narrow filtering. The other high precision receiver however starts showing extreme position outliers near the jammer, in excess of 100 m.

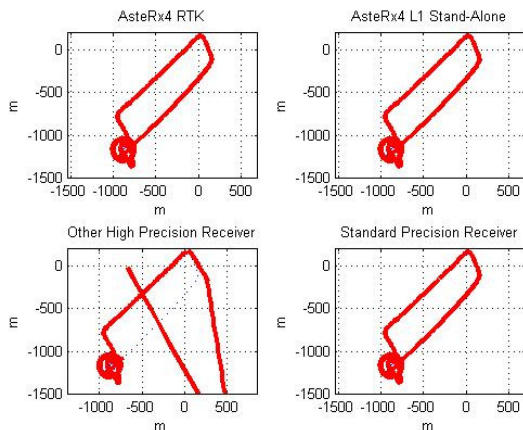


Figure 21: Flight track when exposed to advanced chirp jammer. Jammer is at (0, 0)

The C/No of a high-elevation satellite is shown in [Figure 22](#). The AsteRx4 receiver and the L1 receiver are only showing a minor impact on the L1C/A C/No. The other

high-precision receiver shows a huge drop in C/No. This is surprising, as AsteRx4 keeps on tracking the signal with less than 6 dB C/No loss if all interference mitigation is disabled. We believe this is because the other receiver has a wide-band architecture with little sub-band filtering, making sub-bands like GPS L1 vulnerable to interference in e.g. the GLONASS L1 band or Inmarsat L-band.

[Figure 22](#) also shows the GPS L2P C/No. Although the chirp jammer is jamming the L2 band, it is sufficiently cancelled by the adaptive filter to allow codeless P-code tracking.

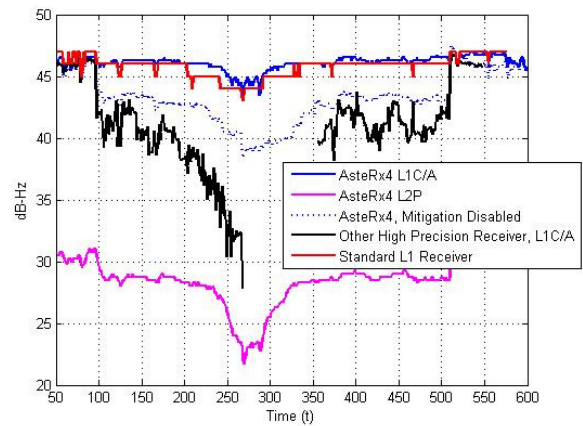


Figure 22: C/No when exposed to advanced chirp jammer

CW JAMMERS

Continuous wave jammers are targeting the main lobe of the L1 C/A signal. We simulated a CW jammer with a standard lab signal generator. The frequency was tuned to 1575 MHz, near the L1 center frequency. The power level of the initial test was 10 mW, equal to the first L1 chirp jammer.

This resulted in the flight tracks of [Figure 23](#). The AsteRx4 flight tracks show no visible effect of the jammer. The other high-precision receiver loses navigation during a large part of the flight. The flight track of the L1 receiver is surprisingly good at first sight. It should be remarked that this receiver is advertised to have CW-interference mitigation.

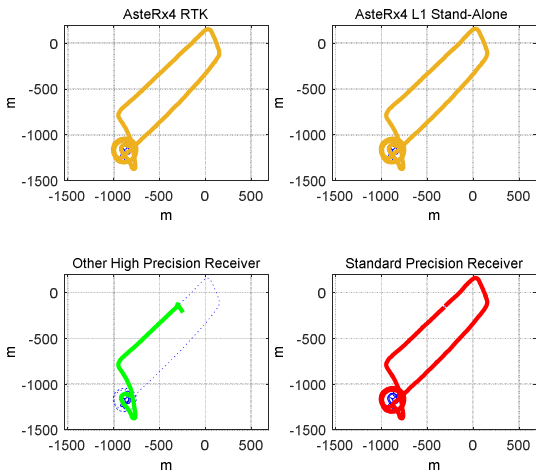


Figure 23: Flight track when exposed to 10-mW CW jammer. Jammer is at (0, 0)

However, when analyzing the 3D error during the most challenging part of the flight the L1 receiver shows inaccuracies of several meters (Figure 24), whereas the AsteRx4 receiver shows no degradation of the RTK or stand-alone solution.

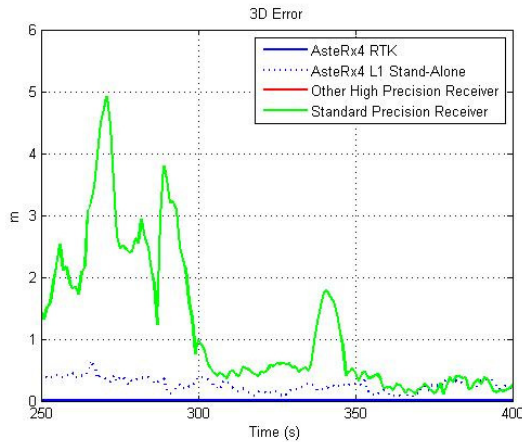


Figure 24: 10-mW CW jammer, 3D positioning error during critical flight phase

This is further clarified by the C/No plot (Figure 25). The AsteRx4 receiver doesn't show any L1 C/No degradation. AsteRx4 automatically assigned a notch filter to the interference frequency, completely rejecting the interference. The other high precision receiver shows an immediate C/No drop if the jammer is enabled (around 100 s) and rapidly loses track when the UAV approaches the jammer. The L1 receiver shows little degradation until an interference level of about -90 dBm, after which the C/No rapidly drops. It even loses the signal momentarily in the

turns, during which the interference level increases a few dB.

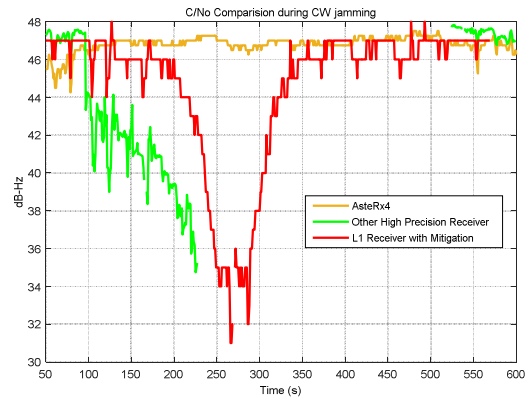


Figure 25: C/No during 10-mW CW jamming

The L1 receiver clearly has a form of interference mitigation, but the dynamic range is limited.

AsteRx4 can handle much higher levels of interference. Even if the CW transmit power is increased to 1 Watt, it still tracks all satellites with less than 10 dB loss at the worst point of the flight (Figure 26). The receiver reports a correct RTK position during the complete flight, except in the turns in the far end. Inspection shows the RTK float solution in the turns is still cm-level accurate.

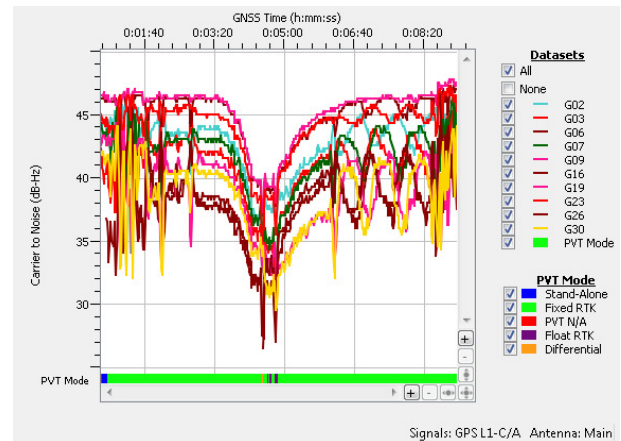


Figure 26: AsteRx4 C/No when CW jammer power is increased to 1 Watt

CONCLUSION

This paper discussed the effect of interference on UAV systems. Both self-interference sources and external interferences have been discussed.

It has been shown that UAV electronics can be a major source of interference to the GNSS receiver, because of the

proximity of the GNSS antenna. Examples of self-interferences from UAV on-board cameras, logging memory and control systems have been studied in the time and frequency domain with the help of a receiver built-in RF monitor.

Regarding the external interferences, it has been shown that low-power inexpensive chirp or CW jammers can compromise the UAV operation, even when they are hundreds of meters away. Interference mitigation in the GNSS receiver has been shown to dramatically reduce the effect of such interferences.

ACKNOWLEDGMENT

The authors thank their colleagues David Feng (Septentrio, Inc) and Marnix Volkaert (Septentrio NV) for their assistance with the simulator tests.

REFERENCES

1. *DME/TACAN interference mitigation for GNSS: algorithms and flight test results*, Grace Xingxin Gao, http://gracegao.ae.illinois.edu/publications/journal/2013_GPS%20solutions_DME.pdf
2. *First Field Experience with L5 signals: DME Interference Reality Check*, A. Simsky, W. De Wilde, T. Willems, D. Mertens, E. Koitsalu, JM Sleewaegen, Proceeding of ION GPS, September 2009.
3. *Characterization of L5 Receiver Performance Using Digital Pulse Blanking*, J. Grabowski, C. Hegarty, Proceedings of ION GPS 2002, Portland, OR, September 2002.
4. FCC Title 47, part 15
5. *Sentinel project: report on GNSS vulnerabilities*, Chronos Technology, April 2014, http://www.chronos.co.uk/files/pdfs/gps/SENTINEL_Project_Report.pdf
6. *Car jammers: interference analysis*, R. Bauernfeind, T. Kraus, D. Dötterböck, B. Eissfeller, E. Loehnert, and E. Wittmann, GPS world, 1 October 2011, <http://gpsworld.com/transportationroadcar-jammers-interference-analysis-12128/>
7. Aggarwal, P., Syed, Z., Noureldin, A., El-Sheimy, N., *MEMS-Based Integrated Navigation*, Artech House, 2010